Am J Cancer Res 2025;15(2):546-558
www.ajcr.us /ISSN:2156-6976/ajcr0162927

Original Article

Plasma exosomal miR-150-3p, *NMT2*, and *PRDM1* as predictive biomarkers of acute tumor response in patients with cervical cancer undergoing chemoradiotherapy

Oyeon Cho

Gynecologic Cancer Center, Department of Radiation Oncology, Ajou University School of Medicine 164, World Cup-ro, Yeongtong-gu, Suwon 16499, Korea

Received December 25, 2024; Accepted February 5, 2025; Epub February 15, 2025; Published February 28, 2025

Abstract: Locally advanced cervical cancer (LACC) is primarily treated with weekly cisplatin-based concurrent chemoradiotherapy (CCRT); however, predicting acute tumor response remains challenging. This study aimed to identify plasma exosomal microRNAs (miRNAs) and messenger RNAs (mRNAs) that could predict rapid tumor regression in patients with LACC undergoing CCRT. Overall, 41 patients with stage IB-IVB cervical cancer were included. All patients received CCRT, and plasma exosomal RNA samples were collected before treatment and 2 weeks after radiation therapy (RT). Acute tumor response (AR) was defined as the regression rate of tumor volume (TV) (cm^3) measured at the fourth week of treatment compared with the initial TV (iTV). The $\log_2$ fold change of miRNA and mRNA was calculated by comparing RNA read counts before and after the second week of CCRT for each patient. A correlation matrix identified RNAs associated with AR. The selected RNAs were validated through linear regression and Wilcoxon rank-sum tests. Leave-one-out cross-validation was performed in subgroups based on iTV. miR-150-3p, *NMT2*, and *PRDM1* were identified as key predictors of AR, demonstrating significant associations with immune-mediated tumor responses. A decrease in post-RT levels of these RNAs was significantly associated with poor AR, particularly in patients with large iTVs. The predictive model combining miR-150-3p, *NMT2*, and *PRDM1* showed strong correlation with AR ($R^2 = 0.831$, $P < 0.0001$) in the test dataset and was validated in an independent cohort ($R^2 = 0.496$, $P = 0.006$). Cross-validation indicated the robustness of these biomarkers in predicting AR across varying TVs. These findings highlight the potential of plasma exosomal miR-150-3p, *NMT2*, and *PRDM1* are promising biomarkers for predicting AR in patients with LACC undergoing CCRT. These findings could facilitate personalized RT strategies and improve patient outcomes. Further multicenter studies are warranted to validate these biomarkers in larger, diverse cohorts.

Keywords: Cervical cancer, chemoradiotherapy, acute tumor response, plasma exosome, microRNA, messenger RNA, tumor biomarkers, personalized radiation therapy, immune-mediated tumor response, predictive modeling

Introduction

Locally advanced cervical cancer (LACC) is commonly treated with weekly cisplatin-based concurrent chemoradiotherapy (CCRT), comprising external beam radiation therapy (EBRT) followed by intracavitary brachytherapy (ICBT) [1]. However, inadequate regression of large cervical tumors after EBRT can complicate the effective application of ICBT for residual disease eradication. Conversely, even with sufficient regression of primary tumors or metastatic lymph nodes, EBRT doses exceeding 45-50 Gy are often administered. This underscores the need for predictive markers of acute tumor response to tailor radiation therapy (RT) strategies in patients with cervical cancer.

As most cervical cancer cases are human papillomavirus (HPV)-positive, predicting tumor response to EBRT based on HPV status alone presents limited utility [2, 3]. Therefore, identifying alternative biomarkers for predicting treatment response is crucial. Recent evidence suggests that combining pembrolizumab with CCRT significantly improves progression-free survival

https://doi.org/10.62347/SPQY5709

(PFS) in patients with LACC compared to placebo and CCRT alone (hazard ratio: 0.7, 95% confidence interval: 0.55-0.89, $P = 0.002$) [4]. This finding highlights the pivotal role of lymphocyte-mediated tumor eradication in treatment response, demonstrating the importance of the immune system in cervical cancer therapy.

Immune checkpoint inhibitors (ICIs) targeting cytotoxic T-lymphocyte associated protein-4, programmed cell death protein 1, or programmed death-ligand 1 have demonstrated delayed tumor responses in various cancers, necessitating evaluation criteria beyond standard radiologic assessments [5]. Additionally, some studies suggest that lymphocytes may influence acute tumor responses, as evidenced by sustained absolute lymphocyte counts (ALCs) in patients achieving pathologic complete response following neoadjuvant CCRT for rectal cancer [6, 7]. Therefore, identifying biomarkers associated with immune response is essential for predicting tumor regression after RT.

Exosomes, extracellular vesicles measuring 40-160 nm in size, are secreted by both cancer and normal cells and are involved in intercellular communication and regulation of various physiological processes, including cancer progression, immune modulation, and inflammation [8, 9]. Exosomal microRNAs (miRNAs) play a critical role in modulating inflammatory responses by regulating messenger RNAs (mRNAs) [10]. The abundance of immune cell-derived exosomes in blood enables the identification of treatment-related miRNAs and mRNAs through differential gene expression analysis of exosomal RNA before and after RT in individual patients [11, 12]. By examining mRNAs associated with specific RNAs, the potential biological significance of exosomal RNA can be inferred [12].

In light of the points above, this study aimed to identify and validate biomarkers that predict acute tumor response to RT by analyzing post-RT plasma exosomal RNA levels associated with immune response in patients with cervical cancer.

Material and methods

Study participants

This study was approved by the Institutional Review Board of Ajou University Hospital (approval number: DB-2024-482), and the requirement for informed consent was waived owing to its retrospective design. Initially, 42 patients diagnosed with stage IB-IVB cervical cancer, according to the 2018 International Federation of Gynecology and Obstetrics (FIGO) criteria, were included. The inclusion criteria were receipt of weekly cisplatin-based CCRT and the availability of plasma exosomal RNA data collected from blood samples taken before and 2 weeks after RT (Figure S1). One patient was excluded owing to significant dissimilarity in miRNA expression in the post-RT sample, as observed in hierarchical clustering, resulting in 41 patients being included in the final cohort (**Figures 1** and S2). The diagnosis was histologically confirmed by biopsy, and regional lymph node (LN) and distant metastases (DM) were assessed using magnetic resonance imaging (MRI) and positron emission tomography-computed tomography (PET-CT). Treatment commenced within 1 month following the imaging studies. EBRT was administered using intensity-modulated RT targeting the pelvis or para-aortic LNs. The pelvic RT dose was 45 Gy delivered in 25 fractions, with a simultaneous integrated boost of 120%-130% to regional LN metastases. RT response was evaluated via MRI during the fourth week of pelvic EBRT (36-45 Gy in 20-25 fractions). All patients received a weekly cisplatin regimen (30-70 mg/m^2) for six cycles during RT. The details of three patients with one or two distant metastatic lesions who received EBRT in metastatic sites are described in the Supplementary Methods. Of the 41 patients, 39 underwent ICBT, with one patient substituting ICBT with an EBRT boost and another who declined further treatment (Iridium-192; Gamma Medplus iX; Varian, Palo Alto, CA, USA). After completing treatment, patients were followed up every 3 months. Evaluation of primary cervical tumors, regional LN, and DM included pelvic examination, pap smear tests, tumor markers, MRI, and CT.

Acute tumor response

Acute tumor response to RT (AR) was defined as the regression rate of tumor volume (TV) (cm^3) measured at the fourth week of treatment compared with the initial TV (iTV) measured at diagnosis. The regression rate was calculated as

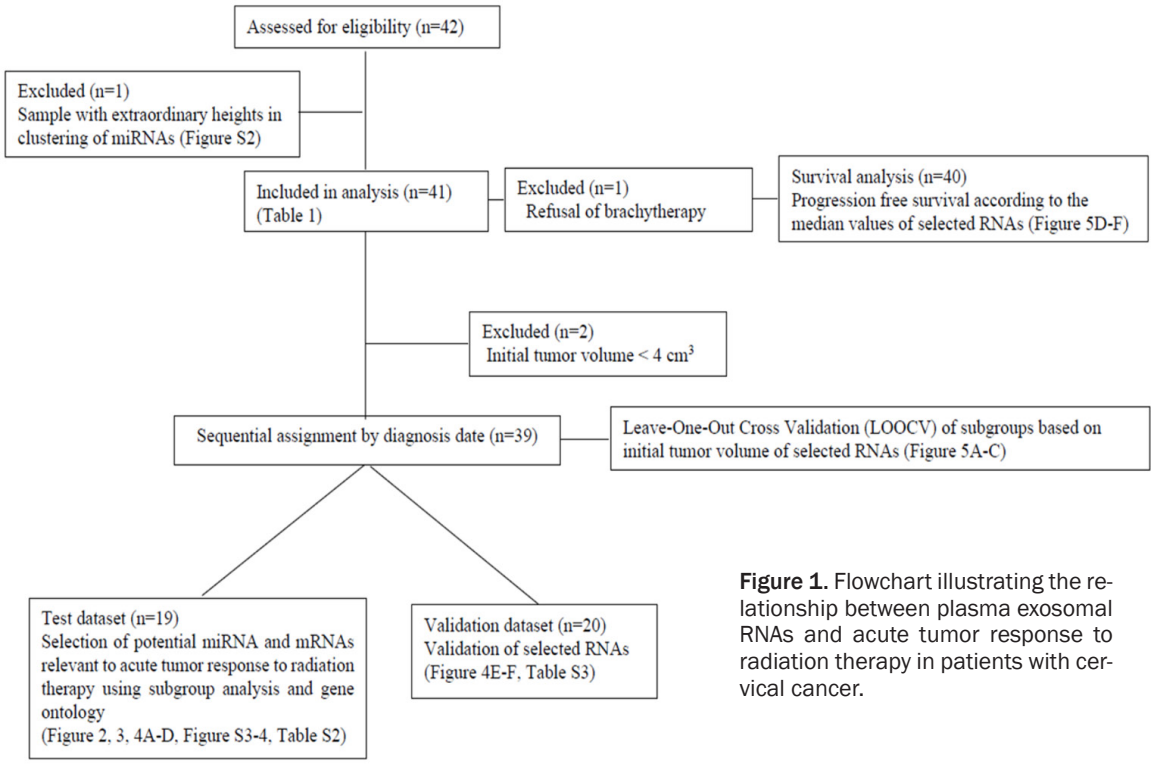

Figure 1. Flowchart illustrating the relationship between plasma exosomal RNAs and acute tumor response to radiation therapy in patients with cervical cancer.

$$AR = \left(\frac{TV\ (cm^3)\ at\ 4th\ week}{TV\ (cm^3)\ at\ diagnosis} \right)$$

TV measurements were obtained using the Eclipse™ version 18.0 Treatment Planning System (Varian). TV was measured using MRI for the primary site, while LN metastatic lesions were assessed using CT or MRI (Figure S1). Measurement of TV was limited to pelvic and abdominal LNs.

Datasets

After excluding two patients with iTVs of < 4 cm^3 from the 41 patients, the remaining 39 patients were divided into a test dataset (n = 19) and a validation dataset (n = 20) based on the chronological order of their diagnostic dates. Plasma exosomal RNAs were selected to predict AR in the test dataset through statistical and biological screening methods. The selected RNAs were validated in another dataset. Cross-validations of subgroups based on iTV were performed using these 39 patients. For survival analysis, 40 patients were included, excluding one who refused further treatment. This process is detailed in **Figure 1**.

Log_2 fold change

The log_2 fold change (Log_2FC) was calculated using next-generation sequencing data from RNAs, including both miRNAs and mRNAs, isolated from plasma exosomes isolated via a polyethylene glycol/dextran aqueous two-phase system (ATPS) (*Exo2D*; ExosomePlus, Seoul, Republic of Korea). Log_2FC values were determined by comparing RNA read counts before (control) and after the second week of CCRT (treatment) for each patient in the cohort, using a trimmed mean of M-value normalization with edgeR after excluding RNAs that were not detected in at least 50% of the samples. This analysis was conducted separately for each dataset. Plasma exosomal RNA sequencing and profiling were conducted by Macrogen (www.macrogen.com) and ROKIT Genomics (www.rokitgenomics.com). Further details are available in the Supplementary Methods.

RNA screening in the test dataset

Pearson's correlations matrix between all variables, including AR and RNAs, was calculated using the "rcorr" function in the "Hmisc" package for R programming (R Foundation for Statistical Computing, Vienna, Austria). miRNAs

associated with AR (|R| > 0.6) were initially selected. The optimal model incorporating the selected miRNAs was identified through an exhaustive search using the "regsubsets" function in the "leaps" package for R. This function evaluates all possible combinations of variables and selects the model with the highest Adjusted R^2 for each variable count. This method was consistently applied throughout the study. To assess the relevance of the sum and difference of the suggested miRNAs to AR, linear regression and the Wilcoxon rank-sum test were performed. A network was constructed using miRNAs related to the selected miRNAs (|R| > 0.4), and the miRNA most strongly associated with AR was identified. Two networks were then created: (1) using mRNAs linked exclusively to the selected miRNA (|R| > 0.6) and (2) incorporating miRNAs within the network, mRNAs associated with AR (|R| > 0.6), and those correlated with both the selected miRNA (|R| > 0.6) and AR (|R| > 0.4). Gene ontology analyses for biological processes and cell types were performed for each network. Among the mRNAs most relevant to AR (|R| > 0.7) within the second network, those demonstrating significant biological relevance based on gene ontology analysis were selected. Key components among the selected RNAs in the network were identified through an exhaustive search using the "regsubsets" function. The relevance of the sum of the finally selected miRNAs and mRNAs to AR was assessed using linear regression and the Wilcoxon rank-sum test. Additional networks were constructed using mRNAs relevant to the selected RNAs (|R| > 0.6), and gene ontology analyses were performed on the RNAs within these networks. Another network was constructed using mRNAs relevant to all the selected RNAs (|R| > 0.4), and gene ontology analyses were conducted on the RNAs within this network. Comparisons were made on the differences in TV at diagnosis (iTV), TV at the 4th week, age at diagnosis, pathology, 2018 FIGO stage, RT field, total dose (TD), ICBT, ALC0 (pretreatment ALC), ALC1 (ALC measured 1 week after RT), ALC2 (ALC measured 2 weeks after RT), and the Log_2FC values of the selected RNAs based on an AR value of 0.2.

Validation dataset

Linear regression and the Wilcoxon rank-sum test were performed to assess the relevance of the sum of the finally selected miRNA and mRNAs to AR in the validation dataset. Comparisons were made on the differences in iTV, TV at the 4th week, age at diagnosis, pathology, 2018 FIGO stage, RT field, TD, ICBT, ALC0, ALC1, ALC2, and the Log_2FC values of the selected RNAs based on an AR value of 0.3.

Cross-validation according to TV

Leave-one-out cross-validations (LOOCVs) were performed using the "trainControl" function from the "caret" package in subgroups based on iTV. The subgroups included patients with iTV values greater than 4, 8, 12, 16, 20, 24, 28, 32, 36, 40, 44, and 48 cm^3.

Survival analysis

The endpoint of the survival analysis was progression-free survival (PFS). The follow-up period was measured from the end of treatment to the last visit or event date. The 3-year PFS (3PFS) between the two patient groups, categorized based on the median value of the selected RNAs, was compared using the Kaplan-Meier method and log-rank tests.

Network

Network analyses were performed using Prim's algorithm of minimum spanning tree in the "igraph" package for R. Positively and negatively correlated edges are shown in red and blue, respectively, and were calculated as Pearson's correlations.

Gene ontology

Enrichment analysis was performed for gene ontology annotation in Enrichr (https://maayanlab.cloud/Enrichr) using the mRNAs that significantly changed based on the log_2FC of the selected RNAs and the RNAs from the network [13].

All data analyses and visualizations were performed using R version 4.4.1 (https://www.r-project.org).

Results

Table 1 presents the characteristics of the patients included in this study.

miR-150-3p as a key component for predicting AR

Figure 2 illustrates the process of selecting miR-150-3p as a key component for predicting

Table 1. Patients' clinical characteristics (all patients)

	All
	N or median [IQR] (N = 41)
Tumor volume at diagnosis (cm^3)	26.20 [16.5; 81.4]
Tumor volume at 4th week (cm^3)	5.50 [1.8; 14.9]
Age (years) [IQR]	50 [46.0; 58.0]
≥ 50	25 (61.0%)
< 50	16 (39.0%)
FIGO stage 2018	
IB	6 (14.6%)
IIB-IIIC1	23 (56.1%)
IIIC2-IVB	12 (29.3%)
Pathology	
Adenocarcinoma	7 (17.1%)
Adenosquamous cell carcinoma	1 (2.4%)
Unknown carcinoma	1 (2.4%)
Squamous cell carcinoma	32 (78.1%)
Radiotherapy field	
Pelvis with paraaortic region	11 (26.8%)
Pelvis	30 (73.2%)
Total dose (EQD2)	76.25 [72.25; 81.75]
≥ 76.25	28 (68.3%)
< 76.25	13 (31.7%)
Intracavitary brachytherapy	
24 Gy in 4 fractions	14 (34.2%)
24 Gy in 6 fractions	10 (24.4%)
25 Gy in 5 fractions	1 (2.4%)
28 Gy in 7 fractions	1 (2.4%)
30 Gy in 6 fractions	13 (31.7%)
EBRT replacement	1 (2.4%)
Refusal	1 (2.4%)
ALC0 (cells/ul) [IQR]	1699.2 [1463.0; 2025.0]
ALC1 (cells/ul) [IQR]#	921.45 [615.2; 1242.55]
ALC2 (cells/ul) [IQR]	509.60 [371.2; 670.0]
miR-150-3p [log_2FC]	-0.67 [-1.58; 0.18]
PRDM1 [log_2FC]	0.13 [-0.7; 1.24]
NMT2 [log_2FC]	-0.17 [-0.71; 0.31]
miR-150-3p+*PRDM1* [log_2FC]	-0.36 [-2.17; 0.74]
miR-150-3p+*NMT2*+*PRDM1* [log_2FC]	-0.48 [-3.23; 1.05]

IQR: interquartile range, FIGO: International Federation of Gynecology and Obstetrics, EQD2: equivalent dose in 2 Gy fractions, EBRT: External Beam Radiotherapy, ALC: absolute lymphocyte counts, ALC0: pretreatment ALC, ALC1: ALC 1 week after EBRT, ALC2: ALC 2 week after EBRT, NMT2: N-myristoyltransferase 2, PRDM1: PR/SET domain 1, #: ALC1 has 1 missing value.

AR in patients with cervical cancer who underwent CCRT in the test dataset.

Among the subsets of combinations using miR-150-3p, miR-424-3p, and miR-3940-3p, which showed significant correlations with AR (|R| > 0.6), all optimal models included miR-150-3p (**Figure 2A**). The seven possible combinations are as follows: miR-150-3p, miR-3940-3p, miR-424-3p; miR-150-3p, miR-424-3p; miR-150-3p, miR-3940-3p; miR-3940-3p, miR-424-3p; miR-150-3p; miR-424-3p; and miR-3940-3p. The models with the highest Adjusted R^2 were selected for each number of explanatory variables: miR-150-3p, miR-3940-3p, and miR-424-3p for three variables; miR-150-3p and miR-424-3p for two variables; and miR-150-3p for one variable. Among these, the combination of miR-150-3p and miR-424-3p was identified as the optimal model due to its highest Adjusted R^2 value. The combination of miR-150-3p and miR-424-3p (log_2FC) showed a strong linear relationship with AR and demonstrated statistically significant differences between patients with poor AR and those with good AR (**Figure 2B** and **2C**). However, when miR-150-3p and miR-424-3p were analyzed separately (**Figure 2D** and **2E**), miR-150-3p was identified as the primary component distinguishing patients with poor response (AR < 0.2) from those with good response (AR ≥ 0.2). Network analysis of miRNAs associated with miR-150-3p or miR-424-3p (miR-miR network) revealed that miR-150-3p was central within this network (**Figure 2F**).

Given that miR-150-3p was the primary miRNA for predicting AR in the test dataset, while miR-424-3p played a supplementary role, and since the goal was to identify miRNAs that can be universally applied to predict acute tumor response, it was appropriate to focus solely on evaluating miR-150-3p.

Selection of lymphocyte-enriched RNAs relevant to AR

The network analysis of mRNAs associated with miR-150-3p (miR-150-3p-mR network) revealed a centralized structure with miR-150-3p at its core (**Figure 3A**). Biological process and cell type annotations of the RNAs within

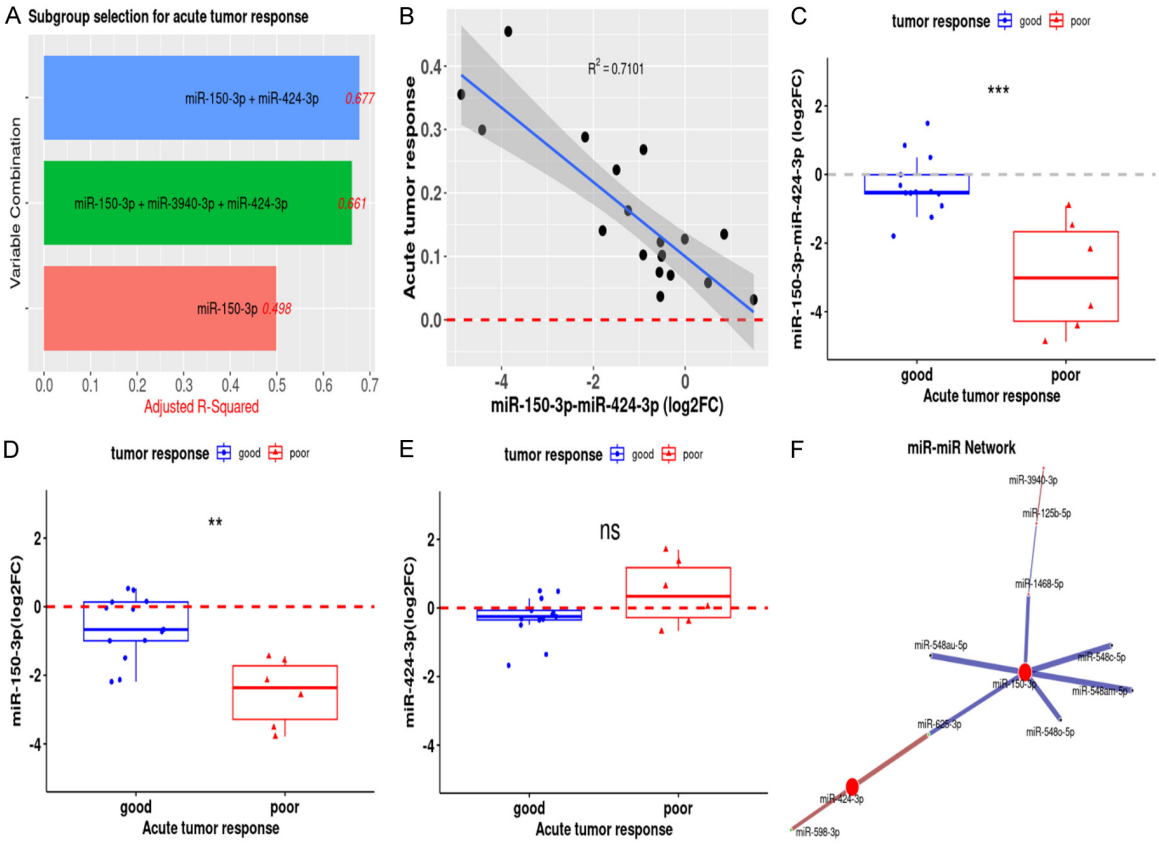

Figure 2. Identification of miR-150-3p as a key microRNA (miRNA) associated with acute tumor response to radiation therapy in the test dataset. (A) Among all possible combinations of three miRNAs, two were selected based on adjusted R^2 values from multiple regression analysis, indicating the strongest association with acute tumor response. (B) A negative linear correlation was observed between the $\log_2$ fold change ($\log_2$FC) difference of the selected two miRNAs and acute tumor response. (C-E) Boxplots comparing the difference between patients with a poor response (acute tumor response ≥ 0.2) and those with a good response (acute tumor response < 0.2): (C) miR-150-3p and miR-424-3p ($\log_2$FC), (D) miR-150-3p ($\log_2$FC), and (E) miR-424-3p ($\log_2$FC). (F) A network analysis of miRNA-miRNA interactions highlighting the central role of miR-150-3p.

this network revealed strong associations with natural killer (NK) cell and T cell-mediated immunity (**Figure 3B**), with a stronger association with mature NK cell-mediated immunity than T cell-mediated immunity. The miR-mR network, defined as the network incorporating miRNAs within the miR-miR network, mRNAs associated with AR, and those correlated with both miR-150-3p and AR, is shown in **Figure 3C**. The network structure comprised three groups of RNAs based on *KMO*, *MYDGF*, and *TLN2* (blue boxes in **Figure 3C**). The biological process and cell type annotations of the RNAs in this network revealed associations with mature T cells, mature NK cell-mediated adaptive immune response, and B cells (**Figure 3D**). The miR-mR network was strongly associated with lymphocyte-mediated immune responses. Among the 17 mRNAs (*CRTAC1, DIABLO, DNAJB5, DPY19L4, E2F3, ERAP2, ESPN, FCER2, MORN3, NMT2, NUP107, PRDM1, PTCD3, QPRT, SLC39A3, TLN2, TRABD*) highly relevant to AR within the miR-mR network (|R| > 0.7), *FCER2*, *NMT2*, and *PRDM1*, along with miR-150-3p, were additionally selected due to their enrichment in lymphocytes from immune cell specificity and blood single-cell data in the Human Protein Atlas (https://www.proteinatlas.org/) [14]. The selection criteria were based on their strong association with AR and biological relevance within the miR-mR network, which showed significant links to lymphocyte-mediated immune responses. The biological process ontology and cell types associated with acute tumor response and miR-150-3p-related mRNAs highlighted robust connections to immune response mechanisms and blood lymphocytes (**Figure 3D**). This indicates that exo-

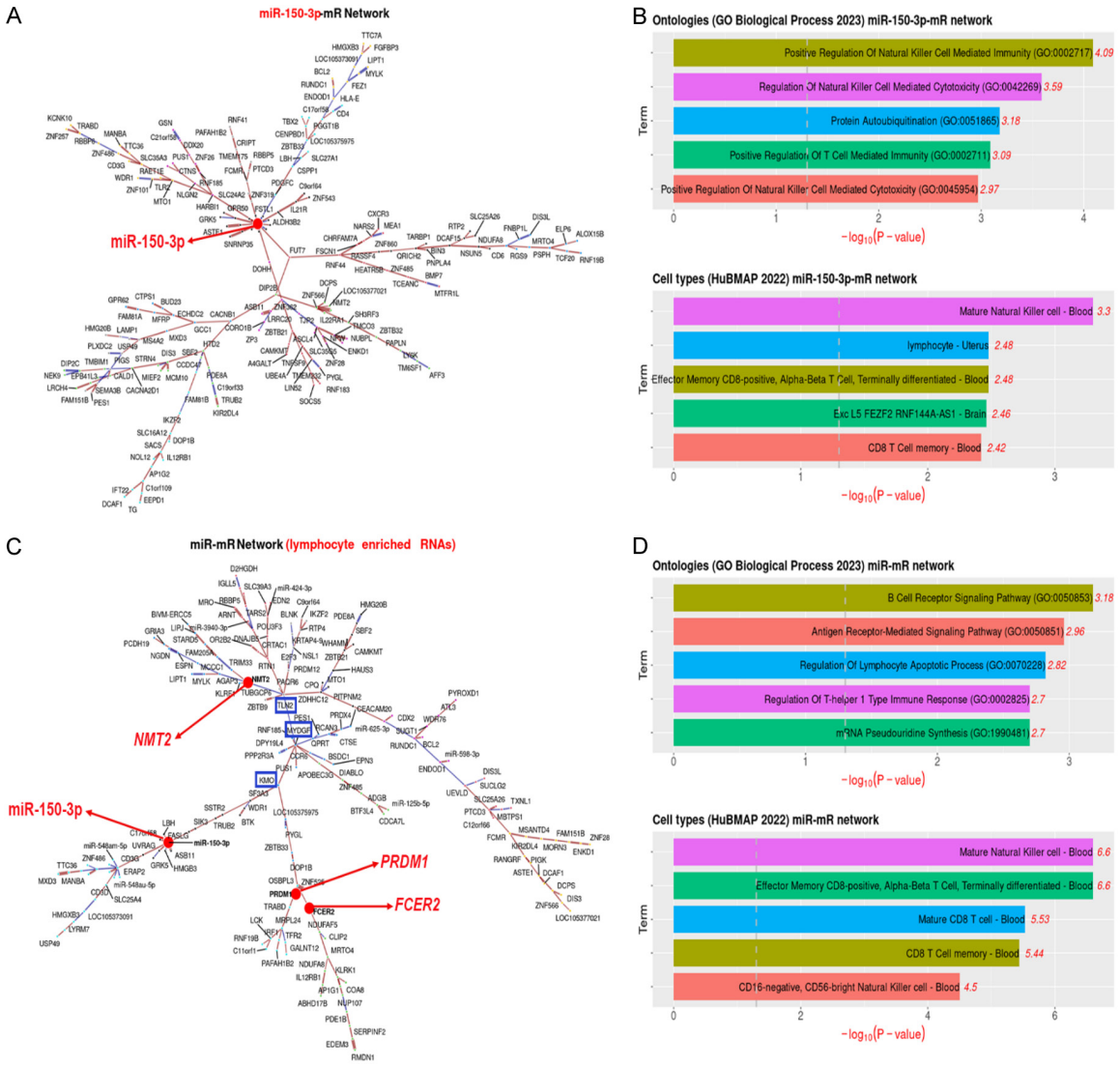

Figure 3. Network analyses of messenger RNAs (mRNAs) associated with miR-150-3p and acute tumor response, highlighting lymphocyte-related ontologies and cell types. A. Network of mRNAs linked to miR-150-3p (red circle). B. Ontologies related to biological processes (upper) and cell types (lower). C. Network of mRNAs associated with both miR-150-3p (|R| > 0.6) and acute tumor response (|R| > 0.4), or with acute tumor response (|R| > 0.6), highlighting lymphocyte-enriched RNAs among them (|R| > 0.7, red circles). D. Ontologies for associated biological processes (upper) and cell types (lower) in the network.

some RNAs associated with AR likely originate from lymphocytes. Among the 17 mRNAs highly associated with AR, *FCER2*, *NMT2*, and *PRDM1* were specifically selected due to their abundance in lymphocytes, ensuring universality and statistical and biological relevance in the context of immune-related mechanisms.

Identification and validation of RNAs for predicting AR

Figure 4 illustrates the process of selecting miR-150-3p, *NMT2*, and *PRDM1* as the final predictors of AR. The combined $\log_2$FC values of miR-150-3p, *NMT2*, and *PRDM1* showed a strong negative correlation with AR (**Figure 4A** and **4B**). The selection process was as follows: the possible combinations were the following 15 subsets: *FCER2*, *NMT2*, *PRDM1*, miR-150-3p; *NMT2*, *PRDM1*, miR-150-3p; *FCER2*, *NMT2*, *PRDM1*; *FCER2*, *NMT2*, miR-150-3p; *FCER2*, *PRDM1*, miR-150-3p; *NMT2*, *PRDM1*; *NMT2*, miR-150-3p; *FCER2*, *NMT2*; *PRDM1*, miR-150-3p; *FCER2*, miR-150-3p; *FCER2*, *PRDM1*; *NMT2*; *FCER2*; miR-150-3p; and *PRDM1*. The values shown in **Figure 4B** represent the mod-

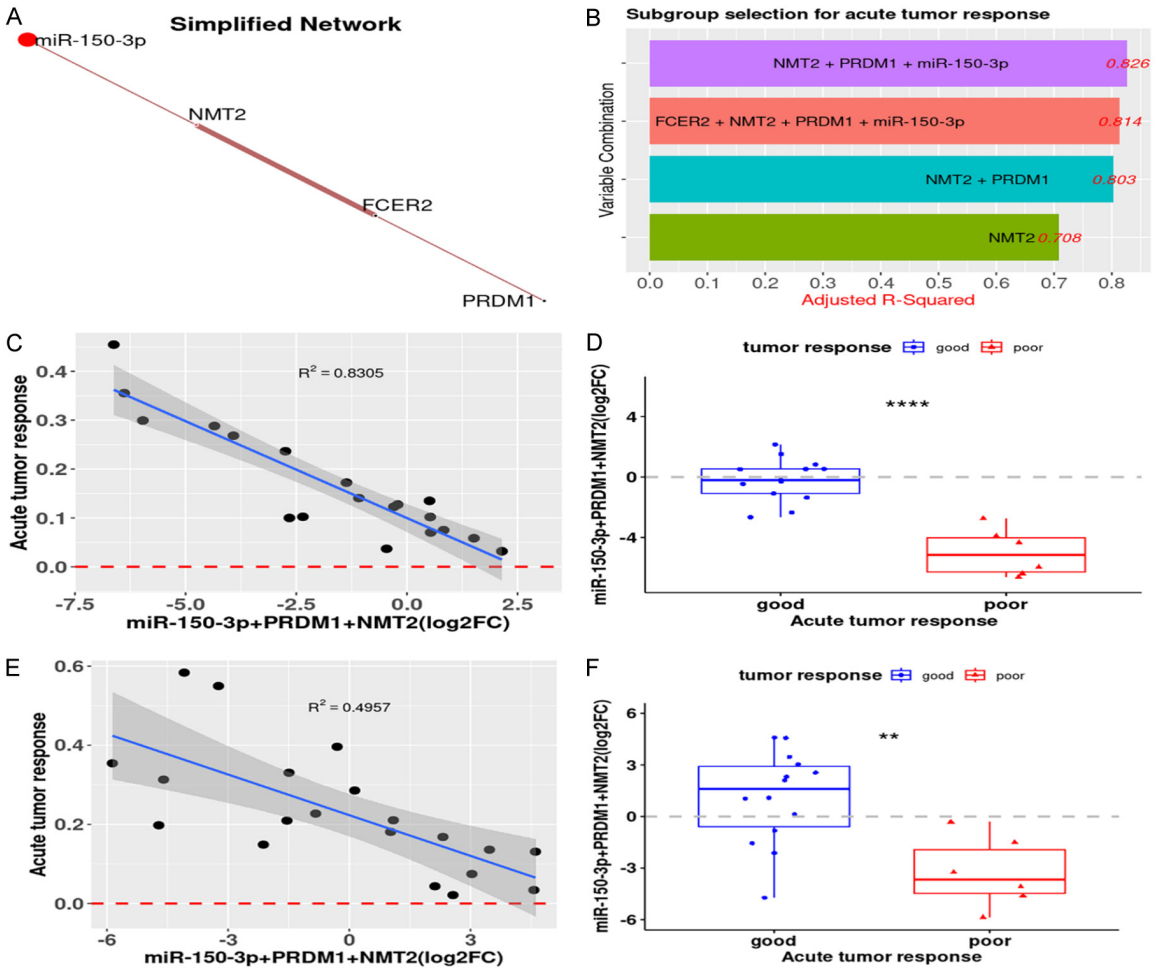

Figure 4. Identification and validation of combinations of miR-150-3p, PRDM1, and NMT2. A. Simplified network highlighting selected four RNAs. B. Three combinations, including one miRNA and three mRNAs, were identified through multiple regression analysis of all possible combinations, demonstrating the strongest association with acute tumor response based on adjusted R^2 values. C. A negative correlation was observed between the combined log_2 fold change (log_2FC) of miR-150-3p, *PRDM1*, and *NMT2* and acute tumor response. D. Boxplot showing a significant difference in miR-150-3p + *PRDM1* + *NMT2* (log_2FC) between patients with a poor response (acute tumor response ≥ 0.2) and a good response (acute tumor response < 0.2). E. The validation dataset confirmed a negative correlation between miR-150-3p + *PRDM1* + *NMT2* (log_2FC) and acute tumor response. F. Validation dataset boxplot showing a significant difference in miR-150-3p + *PRDM1* + *NMT2* (log_2FC) between patients with a poor response (acute tumor response ≥ 0.3) and good response (acute tumor response < 0.3).

els with the highest Adjusted R^2 for each number of explanatory variables: when the model included four variables, *FCER2*, *NMT2*, *PRDM1*, and miR-150-3p were selected; for three variables, *NMT2*, *PRDM1*, and miR-150-3p were selected; for two variables, *NMT2* and *PRDM1* were selected; and for one variable, *NMT2* was selected. Among these, the combination of *NMT2*, *PRDM1*, and miR-150-3p exhibited the highest Adjusted R^2 value and was ultimately chosen as the final model. Additionally, these values showed a significant difference between patients with poor response and those with good response in the test dataset (**Figure 4C**, **4D** and Table S1). In the validation dataset, similar trends were observed (**Figure 4E**, **4F** and Table S2), although the R^2 value for linear regression and the *P*-value for comparison between the two groups were less significant than those of the test dataset (R^2: 0.4957 vs. 0.8305, *P*-value: 0.006 vs. < 0.0001, respectively). The median iTV of the test dataset was approximately three times larger than that of the validation dataset, as shown in Tables S1 and S2 (66.7 vs. 23 cm^3, *P* = 0.006, respectively). In the test dataset, there was a signifi-

cant difference in ALC1 between patients with poor AR and those with good AR (median value: 615.2 vs. 1,001.3 cells/μL, $P = 0.013$, respectively). However, no significant difference was observed in the validation dataset (median value: 784.4 vs. 1,121.55 cells/μL, $P = 0.494$, respectively).

Cross-validations of subgroups based on TV

Figure 5 illustrates the cross-validation of subgroups based on iTV and survival analysis of finally selected RNAs. The R^2 values and root mean squared errors (RMSE) of LOOCV for miR-150-3p + NMT2 + PRDM1 (log_2FC) tended to increase and decrease with the increase in iTV of subgroups but remained consistent between 0.39 and 0.48 for R^2 and between 0.06 and 0.1 for RMSE (**Figure 5B** and **5C**). The R^2 values and RMSE of LOOCV for miR-150-3p (log_2FC) showed a similar pattern, increasing and decreasing with the increase in iTV of subgroups. However, they remained consistent between 0.07 and 0.23 for R^2 and 0.11 and 0.16 for RMSE. For NMT2 (log_2FC), the R^2 values and RMSE tended to decrease with increasing iTV of subgroups but were stable between 0.08 and 0.16 for R^2 and 0.12 and 0.15 for RMSE. The R^2 values and RMSE of LOOCV for *PRDM1* (log_2FC) also tended to increase and decrease with the increase in iTV of subgroups but were consistent between 0.28 and 0.44 for R^2 and 0.09 and 0.13 for RMSE. There was no significant difference in 3PFS between patients with lower log_2FC values than the median and those with higher log_2FC values for miR-150-3p, *NMT2*, and *PRDM1,* as shown in **Figure 5D-F**, respectively. The 3PFS rates were 69.6% vs. 80% for miR-150-3p ($P = 0.5$), 69.6% vs. 80% for *NMT2* ($P = 0.54$), and 79% vs. 70% for *PRDM1* ($P = 0.42$).

Evaluation of biological functions of selected RNAs

To explore the potential biological significance of *PRDM1* and *NMT2*, two networks were constructed using mRNAs relevant to *PRDM1* and *NMT2*. The biological processes and cell type annotations of the RNAs within each network were analyzed (Figure S3). The potential biological implications of *PRDM1* and *NMT2* include their roles in T cell-mediated adaptive immune response and migration from lymph nodes and cell killing by CD8+ T cells or NK cells, respectively. The 54 mRNAs relevant to miR-150-3p, *NMT2*, and *PRDM1* suggest a potential involvement in immune activation processes mediated by NK cells or T cells (Figure S4).

Discussion

This study demonstrated that a combined decrease in post-RT levels of miR-150-3p, *NMT2*, and *PRDM1* in plasma exosomes can predict poor AR and may be associated with reduced activation of NK and T cells. This predictive capability is more significant in patients with large iTVs, with *PRDM1* emerging as the strongest predictor, potentially due to its role in T cell activation, highlighting its potential as a key biomarker for AR.

Exosome isolation using ATPS is a rapid and cost-effective method that yields high purity and minimal disruption but requires careful optimization to avoid contaminant co-isolation, which may necessitate additional purification steps [15]. The ATPS used in this study was selected for exosome isolation because it offers rapid results and ease of use, along with a higher recovery rate (70% vs. 5%-20%) and similar purity (77.5% vs. 70%-90%) compared to ultracentrifugation [16]. Using log_2FC to quantify RNA level changes facilitates detailed gene ontology analysis, overcoming the limitations of traditional group comparisons [17].

The decreased log_2FC value of miR-150-3p consistently predicted poor AR across the test, validation, and LOOCV datasets. Gene ontology analysis of related mRNAs suggested that miR-150-3p was more associated with mature NK cell-mediated immune responses rather than T cell responses. Additionally, the LOOCV results showed that miR-150-3p exhibited a stronger predictive ability in patients with iTV > 25 cm^3, contributing to the increased combined log_2FC values of miR-150-3p, NMT2, and PRDM1. Previous studies have indicated that elevated miR-150 levels can promote mature NK cells and suppress immature NK cells, while miR-150-5p can reduce NK cell cytotoxicity by targeting perforin-1 [18, 19]. These findings suggest that miR-150-5p promotes the development of mature NK cells but suppresses their cytotoxicity against tumor cells. However, our study indicated that higher post-RT levels of miR-150-3p, another mature miRNA derived

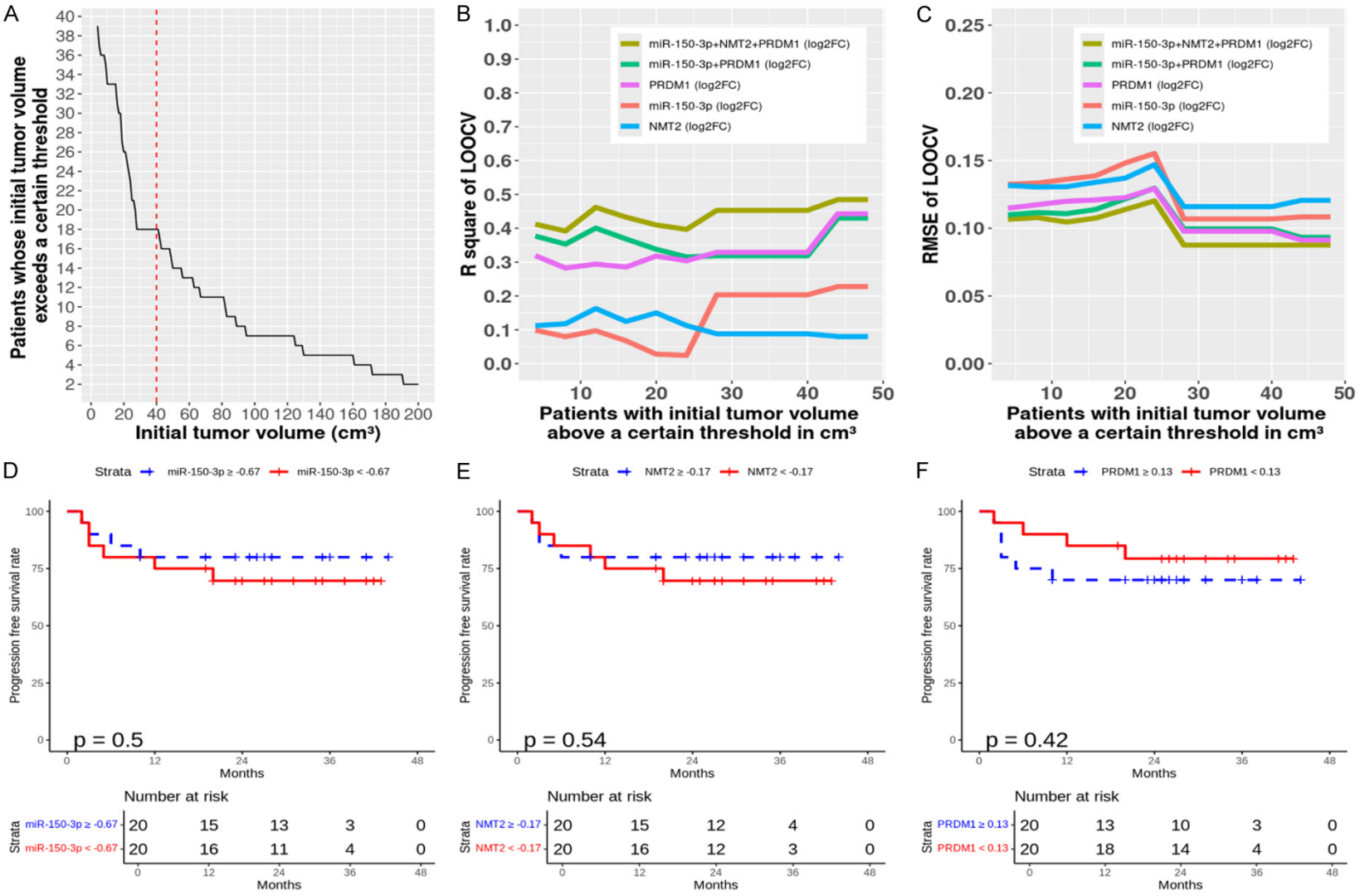

Figure 5. Cross-validation of subgroups based on initial tumor volume and survival analysis of finally selected RNAs. (A) The number of patients stratified into subgroups based on initial tumor volume. (B) R^2 values. (C) Root mean squared error (RMSE) from leave-one-out cross-validation (LOOCV) of selected RNAs in subgroups of patients with initial tumor volumes above specific thresholds. (D-F) Kaplan-Meier plots and log-rank tests comparing progression-free survival between two patient groups divided by the median value of log_2 fold change (log_2FC) values of (D) miR-150-3p, (E) *NMT2*, and (F) *PRDM1*, respectively.

from the miR-150 precursor, may enhance both the number and cytotoxicity of NK cells, especially in patients with large iTV. Notably, no studies to date have examined miR-150-3p's role in lymphocytes, including NK cells.

Myristoylation, mediated by the enzyme N-myristoyltransferase (encoded by *NMT1* or *NMT2*), involves attaching a myristoyl group to the N-terminal glycine of a protein, crucial for its membrane targeting and function [20]. This process plays a key role in T cell viability, activation, and the induction of extrinsic apoptosis in target cells by cytotoxic T cells [21]. During apoptosis, cleaved BID undergoes N-myristoylation by caspase 8, targeting BID to the mitochondria and enhancing its pro-apoptotic function [22]. Therefore, the decreased $\log_2$FC values of *NMT2* observed in this study may indicate a reduced capacity of CD8 T cells to induce apoptosis. This role related to the cytotoxicity of *NMT2* may also apply to the extrinsic apoptosis pathway of target tumor cells induced by mature NK cells [23].

PRDM1, identified as the primary predictor of AR among the three selected plasma exosomal RNAs, plays a critical role in T cell migration and maturation, likely originating from lymph nodes or the thymus [24]. This suggests that CD8 T cells attack tumor cells through adaptive immune responses mediated by *PRDM1*. Notably, patients with increased post-RT levels of *PRDM1* tended to have lower PFS than those with decreased levels, contrasting with patterns observed for miR-150-3p and *NMT2*. Blimp-1, encoded by the *PRDM1* gene, is essential for CD8 T cell differentiation and migration to inflammatory sites while directing CD4 T cells toward Th2 differentiation and inhibiting other lineages [24, 25]. Furthermore, Blimp-1 is significantly upregulated in exhausted CD4 and CD8 T cells under chronic antigen stimulation from infections or cancer [24, 26]. Increased *PRDM1* levels post-RT may initially indicate active cancer cell eradication by CD8 T cells, as RT enhances the exposure of immunogenic antigens [27]. However, chronic stimulation can lead to Th2 differentiation and T cell exhaustion, disrupting normal immune function. The presence of residual tumors after CCRT could further facilitate disease progression, especially with elevated *PRDM1* levels. Conversely, low *PRDM1* levels may promote a delayed but sustained immune response against residual tumors despite poor AR. This suggests that ICIs like pembrolizumab may be more effective for patients having LACC with low post-RT *PRDM1* levels, while those with high levels may need alternative strategies to address T cell exhaustion. A recent study demonstrated that *PRDM1*-knockout chimeric antigen receptor (CAR) T cells can enhance persistence and therapeutic response by promoting early memory T cell expression and preventing terminal differentiation under repeated stimulation [28]. This highlights the potential of *PRDM1*-ablated CAR T cells as a breakthrough in CAR T cell therapy for solid tumors, especially in cases where residual tumors are resistant to ICIs following disease progression after rapid tumor regression and increased *PRDM1* levels post-RT or chemotherapy [29].

The combination of post-RT levels of miR-150-3p, *NMT2*, and *PRDM1* enhances the predictive ability for AR, with accuracy tending to increase in patients with large iTV. These findings suggest that the coordination of innate immunity by NK cells, cytotoxicity, and adaptive immunity by T cells, mediated by the three selected plasma exosomal RNAs as key regulators of these immune responses, can influence rapid regression following RT. This effect appears to be more significant in larger tumors. *PRDM1* stands out as the most predictive among the three RNAs. This may be because it reflects the extent of cytotoxic T-cell activation and migration in response to increased antigen exposure following RT. Larger tumors are likely to present a greater variety of tumor antigens than smaller ones, necessitating CD8 T cell activation through the recognition of new, unmemorized antigens. NK cells can directly kill tumor cells or indirectly support this process by enhancing antigen presentation and promoting the maturation and activation of dendritic cells [30].

Employing miR-150-3p, *NMT2*, and *PRDM1* clinically to predict AR in patients with LACC may allow for a more flexible RT schedule. Elevated post-RT levels of these RNAs could enable a reduction in RT dose to metastatic LNs or pelvic wall lesions or early initiation of ICBT before completing planned pelvic EBRT. Conversely, lower post-RT levels may support dose escalation to ensure adequate coverage

of primary and metastatic lesions without delaying the initiation of ICBT. This approach can be particularly beneficial for large cervical tumors, especially in settings without MRI-guided ICBT, where cervical motion during EBRT can be managed using advanced technologies like setup control, non-invasive ultrasound tracking, and MRI-based online adaptive planning [31, 32].

Despite these promising findings, this study had some limitations. The small sample size may limit the generalizability of results, and larger, multi-institutional studies are required to confirm these findings. The ATPS isolation method, while effective, requires refinement to ensure purity for clinical applications. Additionally, further research is needed to elucidate the causal mechanisms of these RNA changes and their impact on immune modulation and tumor regression. Prospective clinical trials are necessary to validate the utility of miR-150-3p, *NMT2*, and *PRDM1* as biomarkers for AR prediction and personalized treatment strategies in cervical cancer.

Conclusions

Decreased post-RT levels of miR-150-3p, *NMT2*, and *PRDM1* in plasma exosomes serve as predictors of poor AR, particularly in patients with large tumors. The role of *PRDM1*, the most significant predictor, was highlighted in T cell activation. These findings suggest that these RNAs could be valuable biomarkers for personalizing RT strategies. Moreover, potentially combining these biomarkers with immunotherapy could improve patient outcomes. Future research should focus on validating these biomarkers in larger cohorts and clinical trials.

Acknowledgements

This work was supported by the Bio & Medical Technology Development Program of the National Research Foundation (NRF), funded by the Korean government (Ministry of Science and Information and Communication Technology) (grant number: NRF-2018M3A9E8023860). The clinical and processed RNA data documented in this study are available at https://github.com/oyeoncho/ar. All data pertaining to this study are available as raw sequencing data: ArrayExpress (accession numbers: E-MTAB-10215, 10930, 12187).

Disclosure of conflict of interest

None.

Address correspondence to: Dr. Oyeon Cho, Gynecologic Cancer Center, Department of Radiation Oncology, Ajou University School of Medicine 164, World Cup-ro, Yeongtong-gu, Suwon 16499, Korea. Tel: +82-31-219-4195; Fax: +82-31-219-5879; E-mail: oyeoncho@ajou.ac.kr

References

[1] Morris M, Eifel PJ, Lu J, Grigsby PW, Levenback C, Stevens RE, Rotman M, Gershenson DM and Mutch DG. Pelvic radiation with concurrent chemotherapy compared with pelvic and para-aortic radiation for high-risk cervical cancer. N Engl J Med 1999; 340: 1137-1143.

[2] Xing B, Guo J, Sheng Y, Wu G and Zhao Y. Human papillomavirus-negative cervical cancer: a comprehensive review. Front Oncol 2020; 10: 606335.

[3] Spiotto MT, Taniguchi CM, Klopp AH, Colbert LE, Lin SH, Wang L, Frederick MJ, Osman AA, Pickering CR and Frank SJ. Biology of the radio- and chemo-responsiveness in HPV malignancies. Semin Radiat Oncol 2021; 31: 274-285.

[4] Lorusso D, Xiang Y, Hasegawa K, Scambia G, Leiva M, Ramos-Elias P, Acevedo A, Sukhin V, Cloven N, Pereira de Santana Gomes AJ, Contreras Mejia F, Reiss A, Ayhan A, Lee JY, Saevets V, Zagouri F, Gilbert L, Sehouli J, Tharavichitkul E, Lindemann K, Lazzari R, Chang CL, Lampe R, Zhu H, Oaknin A, Christiaens M, Polterauer S, Usami T, Li K, Yamada K, Toker S, Keefe SM, Pignata S and Duska LR; ENGOT-cx11/GOG-3047/KEYNOTE-A18 investigators. Pembrolizumab or placebo with chemoradiotherapy followed by pembrolizumab or placebo for newly diagnosed, high-risk, locally advanced cervical cancer (ENGOT-cx11/GOG-3047/KEYNOTE-A18): a randomised, double-blind, phase 3 clinical trial. Lancet 2024; 403: 1341-1350.

[5] Robert C. A decade of immune-checkpoint inhibitors in cancer therapy. Nat Commun 2020; 11: 3801.

[6] Kitayama J, Yasuda K, Kawai K, Sunami E and Nagawa H. Circulating lymphocyte number has a positive association with tumor response in neoadjuvant chemoradiotherapy for advanced rectal cancer. Radiat Oncol 2010; 5: 47.

[7] Heo J, Chun M, Noh OK, Oh YT, Suh KW, Park JE and Cho O. Sustaining blood lymphocyte count during preoperative chemoradiotherapy as a predictive marker for pathologic complete response in locally advanced rectal cancer. Cancer Res Treat 2015; 48: 232-239.

[8] Kalluri R and LeBleu VS. The biology, function, and biomedical applications of exosomes. Science 2020; 367: eaau6977.
[9] Kumar MA, Baba SK, Sadida HQ, Marzooqi SA, Jerobin J, Altemani FH, Algehainy N, Alanazi MA, Abou-Samra AB, Kumar R, Al-Shabeeb Akil AS, Macha MA, Mir R and Bhat AA. Extracellular vesicles as tools and targets in therapy for diseases. Signal Transduct Target Ther 2024; 9: 27.
[10] Das K and Rao LVM. The role of microRNAs in inflammation. Int J Mol Sci 2022; 23: 15479.
[11] Li Y, He X, Li Q, Lai H, Zhang H, Hu Z, Li Y and Huang S. EV-origin: Enumerating the tissue-cellular origin of circulating extracellular vesicles using exLR profile. Comput Struct Biotechnol J 2020; 18: 2851-2859.
[12] Cho O. Post-radiotherapy exosomal non-coding rna and hemograms for early death prediction in patients with cervical cancer. Int J Mol Sci 2023; 25: 126.
[13] Kuleshov MV, Jones MR, Rouillard AD, Fernandez NF, Duan Q, Wang Z, Koplev S, Jenkins SL, Jagodnik KM, Lachmann A, McDermott MG, Monteiro CD, Gundersen GW and Ma'ayan A. Enrichr: a comprehensive gene set enrichment analysis web server 2016 update. Nucleic Acids Res 2016; 44: W90-97.
[14] Digre A and Lindskog C. The human protein atlas-Integrated omics for single cell mapping of the human proteome. Protein Sci 2023; 32: e4562.
[15] Iqbal M, Tao Y, Xie S, Zhu Y, Chen D, Wang X, Huang L, Peng D, Sattar A, Shabbir MA, Hussain HI, Ahmed S and Yuan Z. Aqueous two-phase system (ATPS): an overview and advances in its applications. Biological Procedures Online 2016; 18: 18.
[16] Shin H, Han C, Labuz JM, Kim J, Kim J, Cho S, Gho YS, Takayama S and Park J. High-yield isolation of extracellular vesicles using aqueous two-phase system. Sci Rep 2015; 5: 13103.
[17] Cho O, Kim DW and Cheong JY. Screening plasma exosomal RNAs as diagnostic markers for cervical cancer: an analysis of patients who underwent primary chemoradiotherapy. Biomolecules 2021; 11: 1691.
[18] Bezman NA, Chakraborty T, Bender T and Lanier LL. miR-150 regulates the development of NK and iNKT cells. J Exp Med 2011; 208: 2717-2731.
[19] Kim N, Kim M, Yun S, Doh J, Greenberg PD, Kim TD and Choi I. MicroRNA-150 regulates the cytotoxicity of natural killers by targeting perforin-1. J Allergy Clin Immunol 2014; 134: 195-203.
[20] McIlhinney RA. Membrane targeting via protein N-myristoylation. Methods Mol Biol 1998; 88: 211-225.
[21] Udenwobele DI, Su RC, Good SV, Ball TB, Varma Shrivastav S and Shrivastav A. Myristoylation: an important protein modification in the immune response. Front Immunol 2017; 8: 751.
[22] Zha J, Weiler S, Oh KJ, Wei MC and Korsmeyer SJ. Posttranslational N-myristoylation of BID as a molecular switch for targeting mitochondria and apoptosis. Science 2000; 290: 1761-1765.
[23] Abel AM, Yang C, Thakar MS and Malarkannan S. Natural killer cells: development, maturation, and clinical utilization. Front Immunol 2018; 9: 1869.
[24] Fu SH, Yeh LT, Chu CC, Yen BL and Sytwu HK. New insights into Blimp-1 in T lymphocytes: a divergent regulator of cell destiny and effector function. J Biomed Sci 2017; 24: 49.
[25] Rutishauser RL, Martins GA, Kalachikov S, Chandele A, Parish IA, Meffre E, Jacob J, Calame K and Kaech SM. Transcriptional repressor Blimp-1 promotes CD8(+) T cell terminal differentiation and represses the acquisition of central memory T cell properties. Immunity 2009; 31: 296-308.
[26] Collier JL, Weiss SA, Pauken KE, Sen DR and Sharpe AH. Not-so-opposite ends of the spectrum: CD8(+) T cell dysfunction across chronic infection, cancer and autoimmunity. Nat Immunol 2021; 22: 809-819.
[27] Lhuillier C, Rudqvist NP, Elemento O, Formenti SC and Demaria S. Radiation therapy and anti-tumor immunity: exposing immunogenic mutations to the immune system. Genome Med 2019; 11: 40.
[28] Yoshikawa T, Wu Z, Inoue S, Kasuya H, Matsushita H, Takahashi Y, Kuroda H, Hosoda W, Suzuki S and Kagoya Y. Genetic ablation of PRDM1 in antitumor T cells enhances therapeutic efficacy of adoptive immunotherapy. Blood 2022; 139: 2156-2172.
[29] Maalej KM, Merhi M, Inchakalody VP, Mestiri S, Alam M, Maccalli C, Cherif H, Uddin S, Steinhoff M, Marincola FM and Dermime S. CAR-cell therapy in the era of solid tumor treatment: current challenges and emerging therapeutic advances. Mol Cancer 2023; 22: 20.
[30] Jiang H and Jiang J. Balancing act: the complex role of NK cells in immune regulation. Front Immunol 2023; 14: 1275028.
[31] Mahmoud O, Kilic S, Khan AJ, Beriwal S and Small W Jr. External beam techniques to boost cervical cancer when brachytherapy is not an option-theories and applications. Ann Transl Med 2017; 5: 207.
[32] Benitez CM, Chuong MD, Künzel LA and Thorwarth D. MRI-guided adaptive radiation therapy. Semin Radiat Oncol 2024; 34: 84-91.

Supplementary Methods

Patients

Three patients with one or two distant metastatic lesions received additional EBRT as the follow.

1. The patient with a solitary left lung lesion underwent stereotactic body radiation therapy (SBRT) with 48 Gy in four fractions, starting in the fourth week of CCRT.

2. The patient with a left supraclavicular lesion was treated with conformal RT of 55 Gy in 22 fractions, beginning in the first week of CCRT.

3. The patient with both left supraclavicular and right axillary lesions received conformal RT of 40 Gy in 10 fractions, starting in the third week of CCRT.

Plasma exosomal ribonucleic acid (RNA) sequencing process

Plasma preparation and storage: Blood was collected in an ethylenediaminetetraacetic acid tube (purple stopper), stored at 4°C, and centrifuged within 2 h at 13,000 rpm and 4°C for 10 min. The uppermost yellow layer of the centrifuged blood was divided into 300 µl aliquots in sterilized cryotubes; then, the tube cap was labeled according to the assigned blood resource number. For long-term plasma storage, the conditions were pp tube, 0.5-2 ml, and -85 to -60°C. The storage period of the samples before being used for analysis ranged from 3 to 12 months.

Small RNA library construction and sequencing: Exosomes were isolated from human plasma by mixing the plasma with Exo2D RNA solution (Exosomeplus). We chose a clinically applicable method that demonstrated stability and consistently yielded a high quantity of exosomes over time. This method involved the extraction of exosomes using an aqueous two-phase system, which was tailored to the surface characteristics of exosomes (Shin, H., Han, C., Labuz, J. *et al.* High-yield isolation of extracellular vesicles using aqueous two-phase system. *Sci Rep* 5, 13103 (2015). https://doi.org/10.1038/srep13103). This exosome isolation kit guaranteed a particle recovery rate of more than 90%. Particle recovery means that after separation (and concentration) using the Exo2D kit, the exosomes from which impurities have been removed are preserved by more than 90% compared to before separation. The detailed isolation process was performed according to the manufacturer's instructions, attached separately. RNA from plasma-derived exosomes was extracted using the miRNeasy Serum/Plasma Kit (Qiagen, Valencia, CA) according to the manufacturer's instructions, attached separately. The RNA concentration was calculated using Quant-IT RiboGreen (Invitrogen). The RNA size was confirmed using an Agilent RNA 6000 Pico Kit, a Small RNA Kit, and an Agilent 2100 Bioanalyzer (Agilent Technologies, Böblingen, Germany). A total of 10 ng of RNA was isolated from each sample and used to construct sequencing libraries using the Simple Modular Architecture Research Tool (SMART)er small RNA (smRNA)-Seq Kit from Illumina following the manufacturer's protocol. In this method, input RNA is first polyadenylated to provide a priming sequence for an oligo(dT) primer. Copy deoxyribonucleic acid (cDNA) synthesis is primed by the 3' smRNA dT Primer, which incorporates an adapter sequence at the 5'end of each RNA template. It adds non-templated nucleotides that are bound by the SMRT smRNA Oligo-enhanced with locked nucleic acid technology for greater sensitivity. In the template-switching step, PrimeScript RT uses the SMART smRNA Oligo as a template for the addition of a second adapter sequence to the 3'end of each first-strand cDNA molecule. In the next step, full-length Illumina adapters (including index sequences for sample multiplexing) are added during polymerase chain reaction (PCR) amplification. The forward PCR primer binds to the sequence added by the SMART smRNA Oligo, while the reverse PCR primer binds to the sequence added by the 3' smRNA dT Primer. The amplified libraries were purified from 6% Novex tetrabromoethane-polyacrylamide gel electrophoresis gels (Thermo Fisher, MA) to excise bands with a size of approximately 138 bp (over than 18 bp of cDNA plus 120 bp of adaptors). The resulting library of cDNA molecules included the sequences required for clustering on an Illumina flow cell. The libraries were gel purified and validated by checking their size, purity, and concentration on an Agilent Bioanalyzer. The libraries were quantified using quantitative PCR (qPCR) according to the

qPCR Quantification Protocol Guide (KAPA Library Quantification kits for Illumina Sequencing platforms) and qualified using TapeStation D1000 ScreenTape (Agilent Technologies, Waldbronn, Germany). The libraries were then pooled in equimolar amounts and sequenced using an Illumina HiSeq 2500 (Illumina, San Diego, USA) instrument to generate 51 base reads. Image decomposition and quality value calculations were performed using the modules of the Illumina pipeline.

Adapter trimming: The raw sequencing reads of the smRNAs from the different experimental samples were pre-processed and analyzed using miRDeep2. Adapter trimming was performed using the cutadapt program to eliminate the adapter sequences that existed in the reads that were attached to the micro-RNA (miRNA) during the smRNA library construction process. The first 3 nucleotides of all the reads were trimmed to remove extra bases inserted during the SMART template-switching activity process. The adapter sequence and other sequences at the 3' end of the adapter were also removed. If a read matched more than at least first five base pairs of the 3' adapter sequence, it was regarded as an adapter sequence and trimmed from the read.

Trimmed reads should have a minimum of 18 bp in order to be considered reliable for analysis. The remaining reads whose sequences did not match the adapter sequence were classified as non-adapter reads. In this analysis, the trimmed and non-adapter reads were combined and regarded as processed reads for downstream analysis.

Clustering: To minimize sequence uniqueness and computational intensity, processed adapter sequence reads were gathered to form a cluster. This cluster contained reads that showed a 100% match with the sequence identity and read length, and it was assigned a temporary cluster ID along with the number of reads it held. *Ribosomal RNA (rRNA) filtering*

In order to eliminate the effects of large amounts of rRNA, the reads were aligned to the 45S pre-rRNA and mitochondrial rRNA sequences of *Homo sapiens* and matched.

Messenger RNA (mRNA) expression profiling: The reference gene annotation for *Homo sapiens* (GRCh38; release 109.20190607) was retrieved from the National Center for Biotechnology Information. Since the produced read contained not only smRNA but also mRNA, mRNA expression profiling was performed using RSEM (v1.3.1) with options (--estimate- rspd --seed-length 15 --strandedness forward).

Identification of known miRNA reads: Sequence alignment and detection of known and novel miRNAs were performed using the miRDeep2 software algorithm. Prior to performing sequence alignment, the *Homo sapiens* reference genome was indexed using Bowtie (1.1.2) for aligning sequencing reads to the reference sequences. Those reads were then aligned with the mature and precursor miRNA sequences of *Homo sapiens* obtained from miRBase v21. The miRDeep2 algorithm is based on the miRNA biogenesis model; it aligns the reads to potential hairpin structures in a manner consistent with Dicer processing and assigns scores that represent the probability that hairpins are true miRNA precursors. In addition to detecting known and novel miRNAs, miRDeep2 estimates their abundance.

Proportion of miRNA and other RNA types: Uniquely clustered reads were then sequentially aligned to the reference genome using miRBase v21 and non-coding RNA database RNAcentral release 10.0 to identify known miRNAs and other types of RNA.

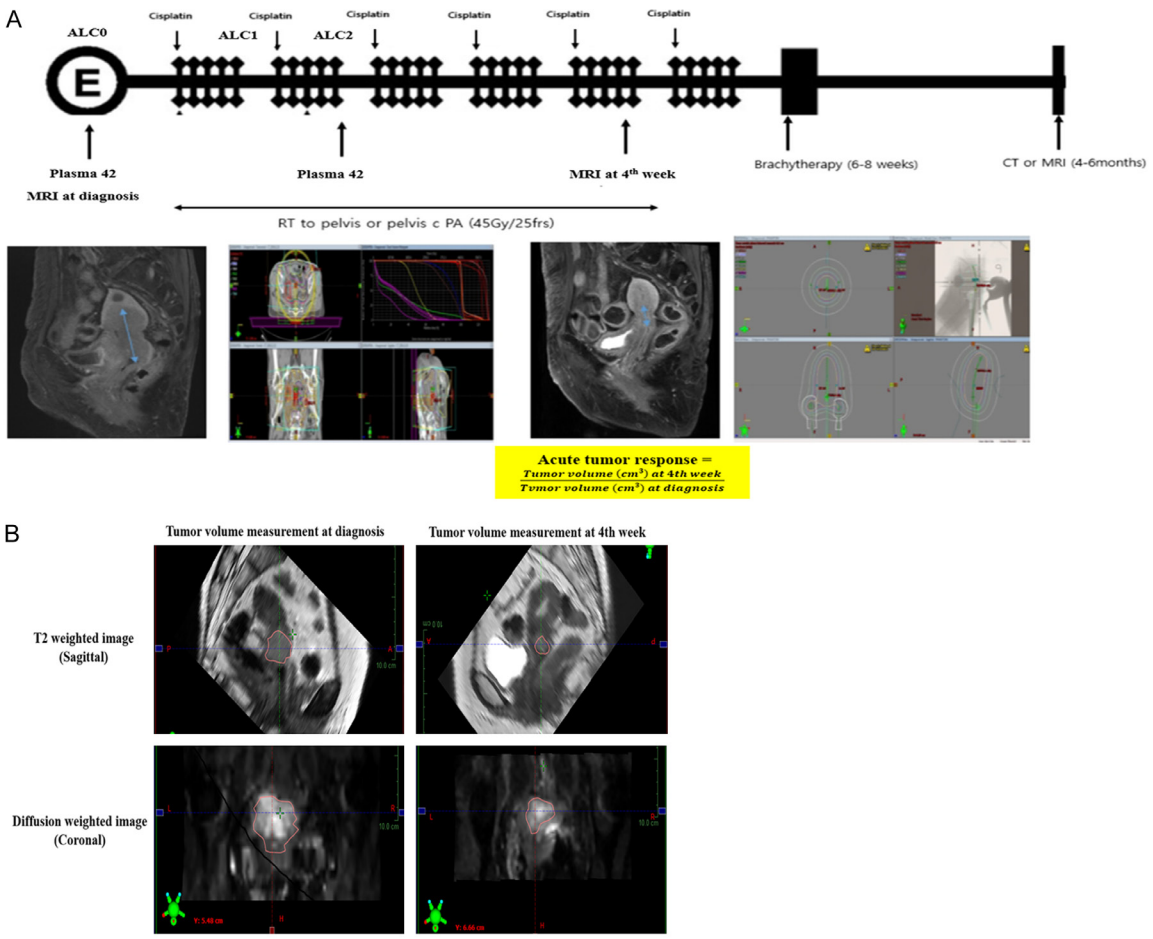

Figure S1. Transcriptomic analysis of RNAs in exosomes isolated from the plasma of 42 patients with cervical cancer. A. Definition of acute tumor response and timeline of blood sampling. B. Measurement of tumor volume of the uterine cervix using magnetic resonance imaging (MRI). EBRT; external beam radiation therapy, ALC; absolute lymphocyte counts, ALC0; pretreatment ALC, ALC1; ALC measured 1 week after EBRT, ALC2; ALC measured 2 weeks after EBRT.

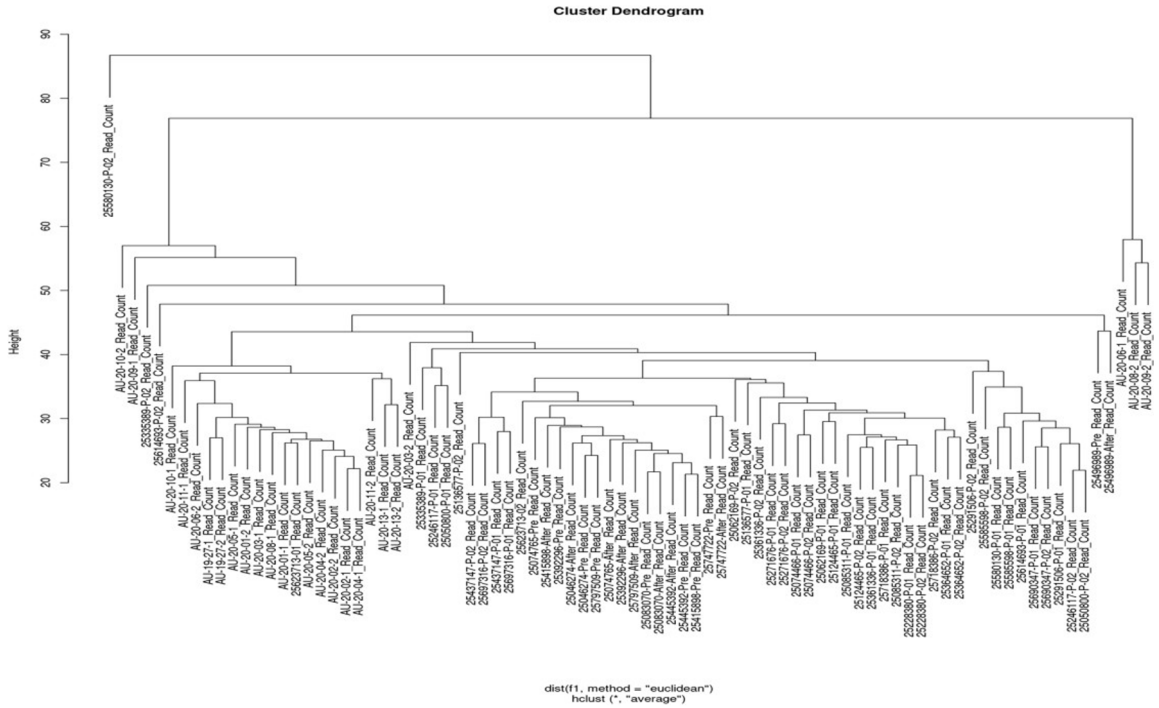

Figure S2. Hierarchical clustering of plasma exosomal miRNA from 84 samples of 42 patients. Dendrogram showing clustering patterns among exosomal miRNAs.

Table S1. Patients' clinical characteristics (test cohort)

	All	Acute tumor response		*P*
	N or median [IQR] (N = 19)	≥ 0.2	< 0.2	
		Poor (N = 6)	Good (N = 13)	
Tumor volume at diagnosis (cm^3)	66.7 [30.85; 127.05]	52.35 [16.5; 124.6]	81.4 [42.7; 129.5]	0.521
Tumor volume at 4th week (cm^3)	9.0 [3.45; 22.8]	19.2 [5.4; 37.3]	8.40 [2.0; 18.2]	0.179
Age (years) [IQR]	50.00 [48.0; 56.5]			0.467
≥ 50	12 (63.2%)	5 (83.3%)	7 (53.9%)	
< 50	7 (36.8%)	1 (16.7%)	6 (46.1%)	
FIGO stage 2018				0.28
IB	2 (10.5%)	0 (0.0%)	2 (15.38%)	
IIIC1	8 (42.1%)	4 (66.67%)	4 (30.77%)	
IIIC2-IVB	9 (47.4%)	2 (33.33%)	7 (53.85%)	
Pathology				0.378
Adenocarcinoma	1 (5.3%)	0 (0.0%)	1 (7.7%)	
Adenosquamous cell carcinoma	1 (5.3%)	0 (0.0%)	1 (7.7%)	
Unknown carcinoma	1 (5.3%)	1 (16.7%)	0 (0.0%)	
Squamous cell carcinoma	16 (84.2%)	5 (83.3%)	11 (84.6%)	
Radiotherapy field				0.979
Pelvis with paraaortic region	8 (42.1%)	2 (33.3%)	6 (46.1%)	
Pelvis	11 (57.9%)	4 (66.7%)	7 (53.9%)	
Total dose (EQD2)	75.5 [72.25; 81.75]			0.515
≥ 75.5	10 (52.6%)	2 (33.3%)	8 (61.5%)	
< 75.5	9 (47.4%)	4 (66.7%)	5 (38.5%)	
Intracavitary brachytherapy				0.557
24 Gy in 4 fractions	2 (10.5%)	0 (0.0%)	2 (15.4%)	
24 Gy in 6 fractions	7 (36.8%)	4 (66.7%)	3 (23.1%)	
25 Gy in 5 fractions	1 (5.3%)	0 (0.0%)	1 (7.7%)	
28 Gy in 7 fractions	1 (5.3%)	0 (0.0%)	1 (7.7%)	
30 Gy in 6 fractions	6 (31.6%)	2 (33.3%)	4 (30.8%)	
EBRT replacement	1 (5.3%)	0 (0.0%)	1 (7.7%)	
Refusal	1 (5.3%)	0 (0.0%)	1 (7.7%)	
ALC0 (cells/ul) [IQR]	1747.2 [1260.7; 2041.2]	1773.25 [1170.0; 1992.6]	1747.20 [1325.4; 2184.0]	0.579
ALC1 (cells/ul) [IQR]#	862.5 [629.8; 1062.4]	615.20 [495.8; 747.0]	1001.30 [814.0; 1277.1]	0.013
ALC2 (cells/ul) [IQR]	419.1 [343.0; 586.45]	358.10 [341.0; 509.6]	516.80 [396.0; 632.4]	0.179
miR-150-3p [log_2FC]	-0.99 [-2.14; -0.06]	-2.36 [-3.52; -1.58]	-0.67 [-0.99; 0.14]	0.002
PRDM1 [log_2FC]	0.15 [-0.51; 0.79]	-0.92 [-1.27; -0.38]	0.75 [0.15; 0.88]	0.001
NMT2 [log_2FC]	-0.44 [-0.99; 0.06]	-1.24 [-2.51; -0.70]	-0.00 [-0.44; 0.09]	0.002
miR-150-3p+*PRDM1* [log_2FC]	-0.74 [-2.49; 0.2]	-3.13 [-3.87; -2.85]	0.11 [-0.74; 0.51]	< 0.001
miR-150-3p+*NMT2*+*PRDM1* [log_2FC]	-1.08 [-3.33; 0.52]	-5.16 [-6.39; -3.92]	-0.21 [-1.08; 0.54]	< 0.0001

IQR: interquartile range, FIGO: International Federation of Gynecology and Obstetrics, EQD2: equivalent dose in 2 Gy fractions, EBRT: External Beam Radiotherapy, ALC: absolute lymphocyte counts, ALC0: pretreatment ALC, ALC1: ALC 1 week after EBRT, ALC2: ALC 2 week after EBRT, NMT2: N-myristoyltransferase 2, PRDM1: PR/SET domain 1, #: ALC1 has 1 missing value.

Table S2. Patients' clinical characteristics (validation cohort)

	All	Acute tumor response		*P*
	N or median [IQR] (N = 20)	≥ 0.3	< 0.3	
		Poor (N = 6)	Good (N = 14)	
Tumor volume at diagnosis (cm^3)	23.0 [13.65; 27.15]	24.5 [18.9; 27.1]	22.1 [8.4; 27.2]	0.536
Tumor volume at 4th week (cm^3)	4.35 [1.75; 7.4]	11.2 [6.7; 14.9]	3.3 [1.6; 4.5]	0.004
Age (years)	50.0 [39.5; 60.5]			0.844
≥ 50	11 (55.0%)	4 (66.7%)	7 (50.0%)	
< 50	9 (45.0%)	2 (33.3%)	7 (50.0%)	
FIGO stage 2018				0.621
IB	2 (10.0%)	0(0.0%)	2 (14.3%)	
IIB-IIIC1	15 (75.0%)	5 (83.3%)	10 (71.4%)	
IIIC2	3 (15.0%)	1 (16.7%)	2 (14.3%)	
Pathology				1
Adenocarcinoma	5 (25.0%)	1 (16.7%)	4 (28.6%)	
Squamous cell carcinoma	15 (75.0%)	5 (83.3%)	10 (71.4%)	
Radiotherapy field				1
Pelvis with paraaortic region	3 (15.0%)	1 (16.7%)	2 (14.3%)	
Pelvis	17 (85.0%)	5 (83.3%)	12 (85.7%)	
Total dose (EQD2)	76.25 [82.25; 81.75]			1
≥ 76.25	13 (65.0%)	5 (83.3%)	12 (85.7%)	
< 76.25	7 (35.0%)	1 (16.7%)	2 (14.3%)	
Intracavitary brachytherapy				0.518
24 Gy in 4 fractions	10 (50.0%)	4 (66.7%)	6 (42.9%)	
24 Gy in 6 fractions	3 (15.0%)	1 (16.7%)	2 (14.3%)	
30 Gy in 6 fractions	7 (35.0%)	1 (16.7%)	6 (42.9%)	
ALC0 (cells/ul) [IQR]	1657.9 [1493.5; 2018.35]	1513.8 [1394.8; 1654.8]	1770.45 [1638.0; 2053.8]	0.179
ALC1 (cells/ul) [IQR]	981.35 [576.0; 1412.8]	782.4 [592.0; 1078.0]	1121.55 [560.0; 1425.6]	0.494
ALC2 (cells/ul) [IQR]	578.25 [425.65; 794.6]	525.0 [395.3; 673.2]	643.15 [456.0; 844.2]	0.602
miR-150-3p [log_2FC]	-0.02 [-1.2; 0.78]	-1.20 [-3.63; -0.61]	0.33 [-0.29; 1.21]	0.015
PRDM1 [log_2FC]	0.42 [-1.4; 1.58]	-0.81 [-2.47; -0.58]	1.37 [-0.05; 1.68]	0.033
NMT2 [log_2FC]	0.05 [-0.6; 0.92]	-0.23 [-0.72; 0.23]	0.19 [-0.43; 1.04]	0.321
miR-150-3p+*PRDM1* [log_2FC]	-0.25 [-1.95; 1.71]	-2.77 [-4.1; -1.54]	1.45 [-0.49; 1.81]	0.002
miR-150-3p+*NMT2*+*PRDM1* [log_2FC]	-0.08 [-2.68; 2.44]	-3.66 [-4.6; -1.5]	1.61 [-0.83; 3.03]	0.006

IQR: interquartile range, FIGO: International Federation of Gynecology and Obstetrics, EQD2: equivalent dose in 2 Gy fractions, EBRT: External Beam Radiotherapy, ALC: absolute lymphocyte counts, ALC0: pretreatment ALC, ALC1: ALC 1 week after EBRT, ALC2: ALC 2 week after EBRT, NMT2: N-myristoyltransferase 2, PRDM1: PR/SET domain 1.

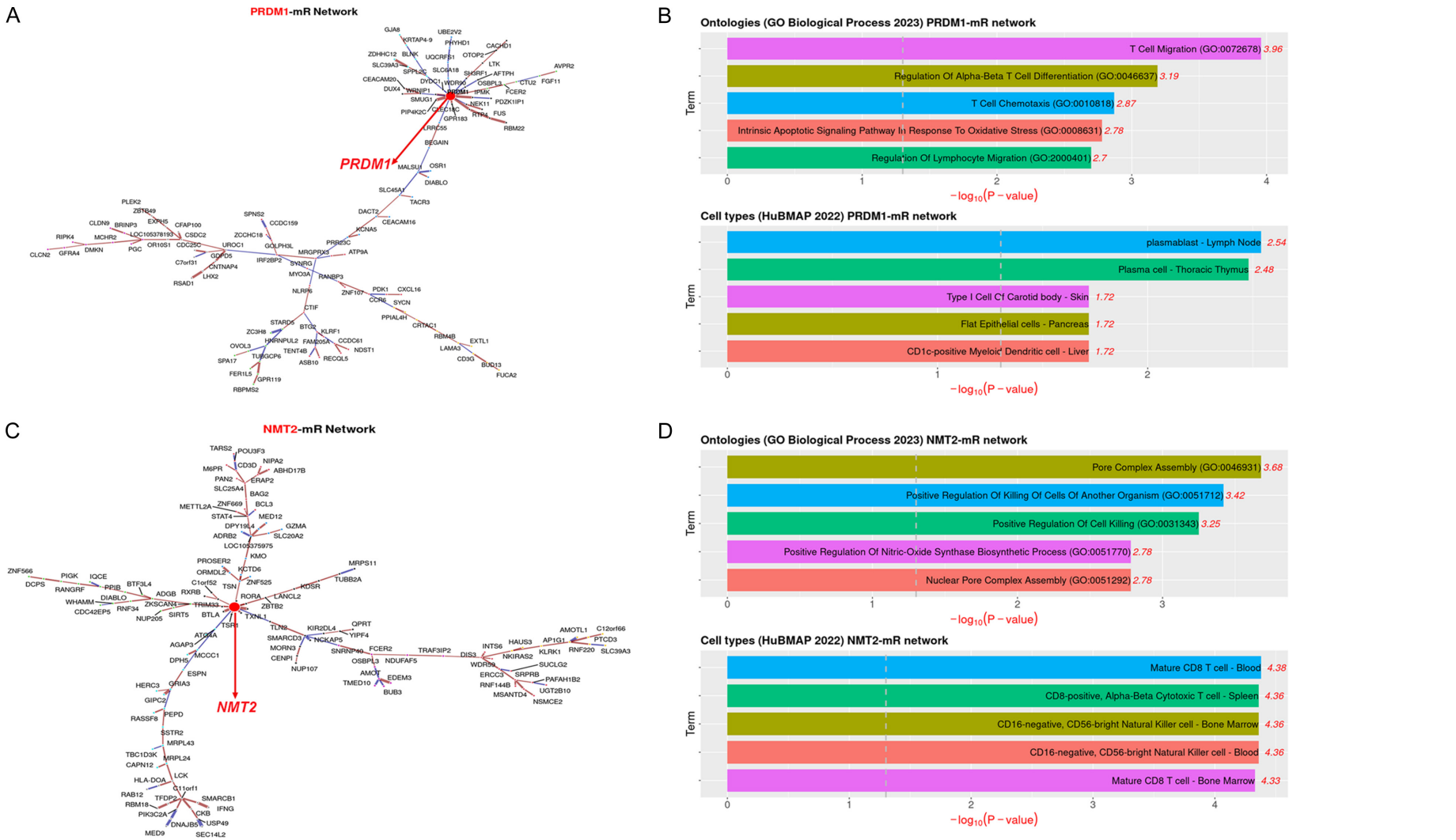

Figure S3. Network analysis of mRNAs associated with *PRMD1* or *NMT2*, highlighting lymphocyte-related ontologies and cell types. (A) Network of mRNAs linked to *PRDM1* (red circle) and (B) ontologies related to biological processes (upper) and cell types (lower). (C) Network of mRNAs linked to *NMT2* (red circle) and (D) ontologies related to biological processes (upper) and cell types (lower).

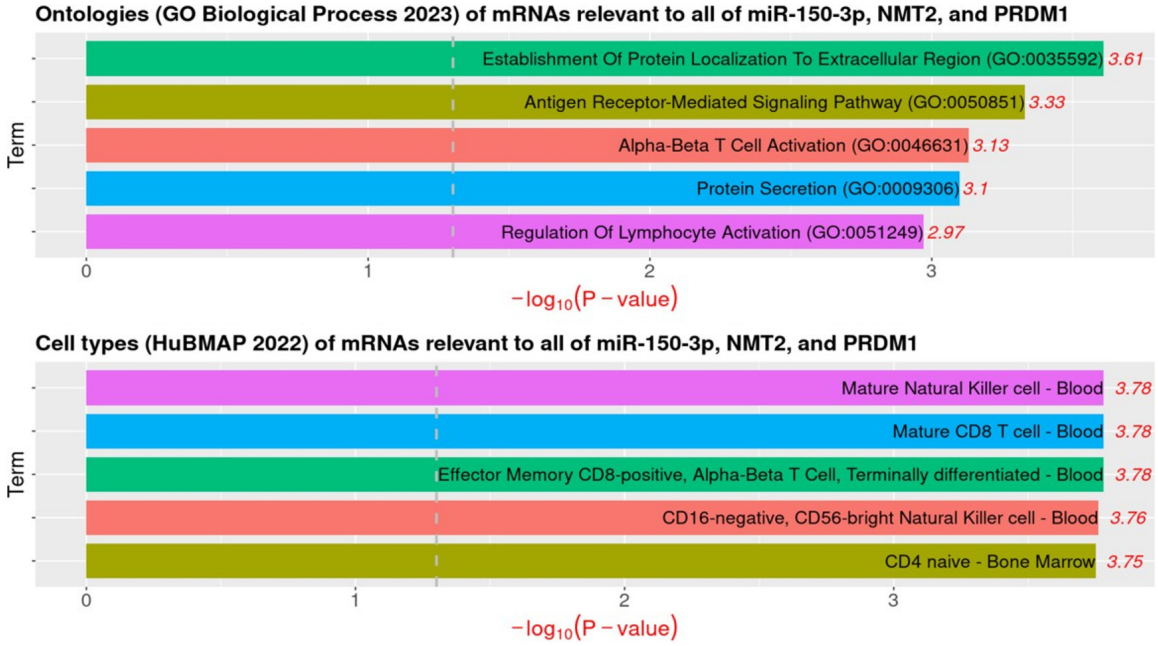

Figure S4. Ontologies related to biological processes (upper) and cell types (lower) using mRNAs related to all of miR-150-3p, *NMT2*, and *PRDM1*.